Journal of Physical Science
Vol. 37(2), 103–121, 2026

Ammonia Gas Sensing Properties of GeO_2:SnO_2/Si Thin Films Prepared via Pulsed Laser Deposition

Mohammed N. Gaser,[1] Hossain M. Moghaddam[1] and Mahdi M. Mutter[2]

[1]Department of Solid-State Physics, Faculty of Basic Sciences, University of Mazandaran, Mazandaran Province, Babolsar, Physics, PM7P+57J, Iran
[2]Scientific Research Commission, Jadriyah Complex, Baghdad, 79GP+7JR, Iraq

Corresponding author: mahdimutter@yahoo.com

Published online: 28 August 2026

To cite this article: Gaser, M. N. et al. (2026). Ammonia gas sensing properties of GeO_2:SnO_2/Si thin films prepared via pulsed laser deposition. *J. Phys. Sci.*, 37(2), 103–121. https://doi.org/10.21315/jps2026.37.2.7

To link this article: https://doi.org/10.21315/jps2026.37.2.7

ABSTRACT: This study investigates the structural, optical and gas sensing properties of tin oxide (SnO_2)-doped germanium oxide (GeO_2) thin films synthesised by pulsed laser deposition (PLD) on Si (111) substrates. Doping concentrations of 2 wt %, 3 wt%, 5 wt% and 8 wt% were employed using a constant laser energy of 350 mJ. The fabricated films were evaluated for ammonia (NH_3) gas sensing at operating temperatures of 200°C, 250°C and 300°C. X-ray diffraction (XRD) analysis confirmed that the deposited films were polycrystalline in nature. The dominant crystalline phases were identified as hexagonal GeO_2 (101) and SnO_2 (110). Scanning electron microscopy (SEM) images revealed a progressive increase in particle size with increasing SnO_2 doping concentration. In contrast, atomic force microscopy (AFM) analysis showed an increase in grain size distribution, surface roughness and root mean square (RMS) values as the SnO_2 content increased. Optical measurements indicated that absorbance increased with higher SnO_2 doping levels, accompanied by a reduction in the optical band gap energy. Gas sensing measurements demonstrated that the GeO_2 film doped with 8 wt% SnO_2 exhibited the best performance, achieving a maximum sensitivity of 16% at 300°C under exposure to 100 ppm NH_3. The optimised sensor also showed fast dynamic behaviour, with a response time (t_res) of 26.1 s and a recovery time (t_rec) of 34.1 s. The remaining GeO_2:SnO_2/Si samples exhibited comparatively lower and varied sensing responses.

Keywords: GeO_2 Nanostructures, GeO_2:SnO_2 thin film, pulsed laser deposition (PLD), gas sensing, direct energy bandgap

1. INTRODUCTION

Semiconductors are the cornerstone of modern technology, driving advancements from microelectronics to renewable energy owing to their tunable electronic and optical properties. This has stimulated intensive research into metal oxide semiconductors (MOS) for cost-effective and high sensitivity gas sensing, which is

crucial for environmental monitoring and industrial safety.[1–3] Rutile germanium oxide (r-GeO_2) is a promising ultra-wide band gap (UWBG) semiconductor with a band gap of approximately 4.7 eV. It is distinguished by its high thermal conductivity and predicted carrier mobility. Unlike many conventional semiconductors, GeO_2 exhibits unique dipolar doping behaviour.[4] Various phases of germanium oxide (GeO_x and GeO_2), in both crystalline and amorphous forms, are widely utilised in applications such as photovoltaic modulators, optical fibres, nonlinear optics and gas sensors due to their favourable optical and electrical properties.[5,6] However, the large band gap and inherently high resistivity of GeO_2 present challenges for scalable device applications. These limitations can be mitigated by optimising stoichiometry and controlling defect chemistry through approaches such as vacancy engineering. Although techniques such as chemical vapour deposition (CVD) and plasma sputtering are commonly employed for GeO_2 film fabrication, they often suffer from limited thickness precision and uniformity.[7–10] Consequently, doping r-GeO_2, particularly with tin oxide (SnO_2), has emerged as an effective strategy to tailor its structural and electronic properties and to promote the formation of oxide heterojunctions.[11–13] In this context, pulsed laser deposition (PLD) offers a highly controlled physical method for fabricating semiconductor and insulating thin films, providing excellent control over thickness and homogeneity.[14,15] Given that ammonia (NH_3) is a widely produced industrial by-product associated with significant toxicity and explosion risks, its detection is of considerable importance.[16,17] This study investigates the synthesis of SnO_2-doped GeO_2 thin films using the PLD technique. The work systematically examines the influence of SnO_2 doping concentration on the structural and optical properties of GeO_2 and establishes a correlation between these modifications and the gas sensing performance toward NH_3. SnO_2-doped GeO_2 thin films were deposited on Si substrates at a laser energy of 350 mJ and characterised using X-ray diffraction (XRD), scanning electron microscopy (SEM), atomic force microscopy (AFM) and optical analysis. Their NH_3 gas sensing performance was subsequently evaluated.

2. EXPERIMENTAL PROCEDURES

GeO_2:SnO_2 thin films were synthesised using a PLD system. High-purity GeO_2 and SnO_2 powders (99.99% purity, supplied by Sigma) were mixed and pressed into targets containing varying SnO_2 concentrations (2 wt %, 3 wt%, 5 wt% and 8 wt%). The deposition process was performed at room temperature (20°C) under a vacuum pressure of 10^{-2} mbar using a Q-switched pulsed laser (DIAMOND-289, λ = 289 nm).[18] Figure 1 shows the PLD system. The laser operating parameters were set to a pulse energy of 350 mJ, a pulse duration of 10 ns, and a repetition rate of 6 Hz, with a total of 100 pulses. The laser beam was focused onto the target at an incident angle of 45°. Prior to deposition, Si (111) substrates were thoroughly cleaned and positioned at a target-to-substrate distance of 3 cm. The film thickness, measured by optical

interferometry, ranged from 259 nm for the undoped GeO_2 sample to 263 nm for the film doped with 8 wt% SnO_2. NH_3 gas sensing measurements were carried out using a custom-built sensing system equipped with a UNI-T UT81B digital multimeter. The test gases were introduced under controlled flow conditions.

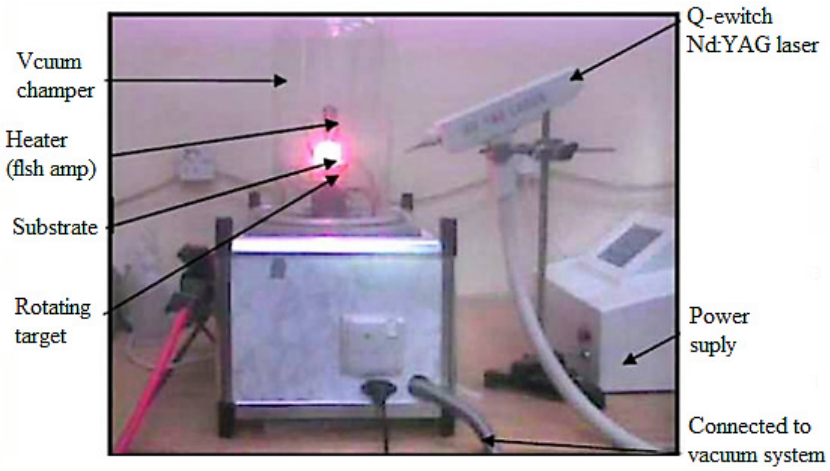

Figure 1: The PLD experimental setup.

2.1 Film Characterisation

XRD analysis was performed using a Philips PW 1055 diffractometer to investigate the structural properties of the GeO_2:SnO_2 thin films. Optical absorption measurements in the wavelength range of 300 nm–800 nm were carried out using a Perkin Elmer UV–Vis spectrophotometer (Model UV-VIS-PV-88). Surface morphology was examined using a JEOL 700 SEM. The gas sensing properties were evaluated using a custom-built sensing system. In addition, X-ray photoelectron spectroscopy (XPS) was conducted with a PHI 5800 ESCA system (47.0.211) to analyse the surface elemental composition and chemical states.

3. RESULTS AND DISCUSSIONS

Figure 2 presents the XRD patterns of pure GeO_2 and GeO_2:SnO_2 thin films deposited by PLD at a laser energy of 350 mJ. The films exhibit a polycrystalline hexagonal phase consistent with JCPDS No. 98-020-0731.[19] Prominent diffraction peaks observed at 2θ values of 20.170°, 26.282° and 41.26° are indexed to the (010), (011) and (102) crystallographic planes, respectively. The sharp and well-defined diffraction peaks indicate good crystallinity and structural ordering of the deposited

films.[20] The crystallite size (D), which represents the size of coherently diffracting domains (typically smaller than the particle size observed in SEM analysis), was estimated using the Debye–Scherrer equation:[20]

$$D = \frac{k\lambda}{\beta \cos\theta} \tag{1}$$

Where, D is the crystallite size (nm), k is the shape factor (0.9), λ is the X-ray wavelength (0.15406 nm for Cu–Kα radiation), β is the full width at half maximum (FWHM) of the diffraction peak (in radians) and θ is the Bragg angle (in degrees). Table 1 shows an increase in crystallite size with increasing SnO_2 doping concentration, which is consistent with the findings reported by Chen et al., (2025).[20]

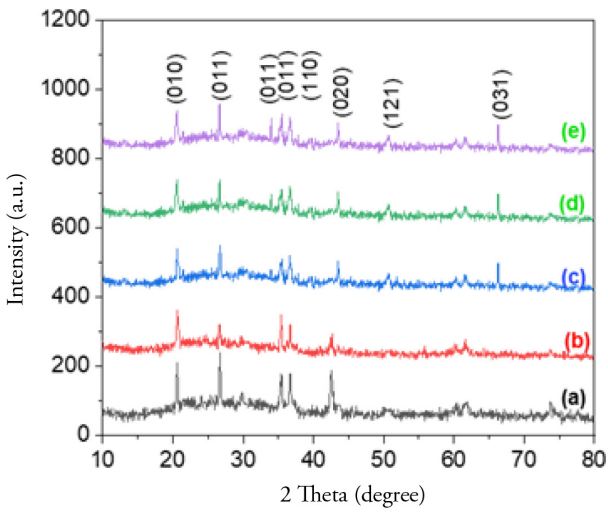

Figure 2: XRD of GeO_2:SnO_2 thin films, (a) GeO_2 pure, (b) GeO_2:2wt%SnO_2, (c) GeO_2:3wt%SnO_2, (d) GeO_2:5wt%SnO_2 and (e) GeO_2:8wt%SnO_2.

Table 1: Crystal structure parameters of GeO_2 on a silicon base at various SnO_2 ratios

Name of sample	2θ (degree)	FWHM (rad)	Crystallite size (nm)	Miller Indices (hkl)	Standard d-spacing (Å)	Experimental d-spacing (Å)	Crystalline system
GeO_2	20.60	0.322	26.70	(010)	4.33	4.30	Hexagonal
	26.91	0.357	25.91	(011)	3.21	3.19	Hexagonal
	36.01	0.301	32.85	(110)	2.45	2.41	Hexagonal
	38.02	0.3	33.84	(102)	3.21	3.20	Hexagonal
	42.01	0.401	26.84	(020)	2.17	2.15	Hexagonal
	Average Crystallite		29.228				
2 wt% SnO_2	20.842	0.353	24.45	(010)	4.322	4.303	Hexagonal
	26.733	0.422	21.22	(011)	3.348	3.360	Hexagonal
	36.121	0.357	29.05	(011)	2.491	2.480	Hexagonal
	36.89	0.343	29.16	(110)	2.385	2.335	Hexagonal
	41.956	0.311	34.59	(102)	2.161	2.150	Hexagonal
	61.51	0.227	73.88	(121)	1.754	1.732	Tetragonal
	Average Crystallite		35.39				
3wt%SnO_2	20.52	0.34	25.12	(010)	4.32	4.29	Hexagonal
	26.74	0.528	17.22	(011)	3.33	3.35	Hexagonal
	36.11	0.356	28.29	(011)	2.48	2.47	Tetragonal
	38.27	0.358	28.46	(110)	2.35	2.3	Hexagonal
	42.87	0.24	45.48	(102)	2.15	2.14	Hexagonal
	50.87	0.27	46.95	(020)	2.40	2.37	Hexagonal
	61.87	0.28	60.60	(121)	1.56	1.51	Tetragonal
	66.04	0.12	164.16	(031)	1.63	1.58	Tetragonal
	Average Crystallite		52.035				
5wt%SnO_2	20.56	0.322	26.53	(010)	4.33	4.30	Hexagonal
	26.90	0.467	19.20	(011)	3.21	3.19	Hexagonal
	36.00	0.321	30.80	(011)	2.45	2.41	Tetragonal
	38.01	0.20	50.76	(110)	3.21	3.20	Hexagonal
	41.23	0.501	21.23	(102)	2.17	2.15	Hexagonal
	50.82	0.28	101.53	(020)	2.40	2.37	Hexagonal
	61.88	0.29	50.22	(121)	1.56	1.51	Tetragonal
	66.04	0.12	164.16	(031)	1.63	1.58	Tetragonal
	Average Crystallite		58.05 nm				

(*continue on next page*)

Table 1: (*continued*)

Name of sample	2θ (degree)	FWHM (rad)	Crystallite size (nm)	Miller Indices (hkl)	Standard d-spacing (Å)	Experimental d-spacing (Å)	Crystalline system
8wt%SnO_2	20.57	0.321	26.61	(010)	4.32	4.28	Hexagonal
	26.93	0.321	27,95	(011)	3.33	3.19	Hexagonal
	36.21	0.311	31.88	(011)	2.47	2.41	Tetragonal
	38.41	0.41	24.90	(110)	3.22	3.20	Hexagonal
	41.33	0.32	33.29	(102)	2.18	2.16	Hexagonal
	50.81	0.21	60.28	(020)	2.39	2.35	Hexagonal
	61.78	0.211	80.18	(121)	1.59	1.54	Tetragonal
	66.24	0.11	180.50	(031)	1.73	1.69	Tetragonal
	Average Crystallite		58.19				

AFM images (see Figure 3) of the GeO_2:SnO_2 thin films demonstrate good adhesion and uniform surface morphology across all samples. As summarised in Table 2, the average surface grain size remains below 106 nm. A clear trend is observed in which the average grain size increases with increasing SnO_2 doping concentration. This behaviour may be attributed to the enhanced ejection of smaller particles from the target surface at higher laser energy, resulting in a higher deposition rate and subsequent coalescence into larger grains on the substrate surface.[23]

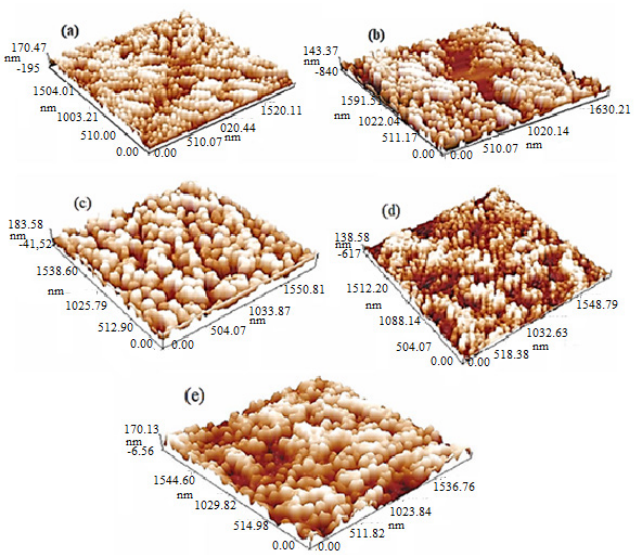

Figure 3: AFM images of GeO_2:SnO_2 thin films at 350 mJ, (a) GeO_2, (b) GeO_2:2wt%SnO_2, (c) GeO_2:3wt%SnO_2, (d) GeO_2:5wt%SnO_2 and (e) GeO_2:8wt%SnO_2.

Table 2: AFM data for GeO_2:SnO_2 thin films at 350 mJ

Samples	Grain size (nm)	Roughness (nm)	Root mean square (nm)
GeO_2	65.01	20.2	25.1
GeO_2:2wt%SnO_2	78.40	38.1	45.7
GeO_2:3wt%SnO_2	92.15	43.5	50.2
GeO_2:5wt%SnO_2	97.07	50.1	56.3
GeO_2:8wt%SnO_2	105.34	56.7	60.4

SEM images (see Figure 4) of the GeO_2:SnO_2 thin films deposited at a laser energy of 350 mJ reveal homogeneous porous structures distributed over the silicon substrate. Particle size analysis indicates a non-monotonic variation with SnO_2 doping concentration. The GeO_2:2 wt% SnO_2 (171.96 nm) and GeO_2:8 wt% SnO_2 (105.22 nm) samples exhibit relatively larger particle sizes, whereas the undoped GeO_2 (60.71 nm) and 5 wt% SnO_2 (18.73 nm) films show comparatively smaller particles. All films display a semi-spherical particle morphology. In general, increasing SnO_2 doping tends to reduce particle size and limit agglomeration. However, the observed agglomeration in the 2 wt% and 8 wt% SnO_2 films may be associated with fluctuations in deposition conditions during the PLD process. These variations in particle size are likely influenced by the interaction between the pulsed laser plume dynamics and the ionic radius of the incorporated Sn^+ ions.[24]

Figure 5 presents the XPS analysis of the GeO_2:2 wt% SnO_2 and GeO_2:8 wt% SnO_2 thin films. As shown in Figure 5a, the Sn 3d spectrum confirms the presence of Sn(IV) species in both samples, with the characteristic Sn $3d_5/_2$ and Sn $3d_3/_2$ peaks located at 486.2 eV and 494.6 eV, respectively.[25] Quantitative XPS analysis revealed notable differences in the surface Sn/Ge atomic ratios, with values of 17% for GeO_2:2 wt% SnO_2 and 7% for GeO_2:8 wt% SnO_2. These results indicate a preferential surface enrichment of Sn species, which may influence crystal growth and structural ordering.[26] Interestingly, the GeO_2:2 wt% SnO_2 sample exhibits more than twice the surface Sn/Ge ratio compared to the 8 wt% SnO_2 film (see Figure 5b). This suggests that at lower nominal doping levels and deposition conditions, Sn species may be more strongly segregated at the surface rather than uniformly incorporated into the film bulk.[27]

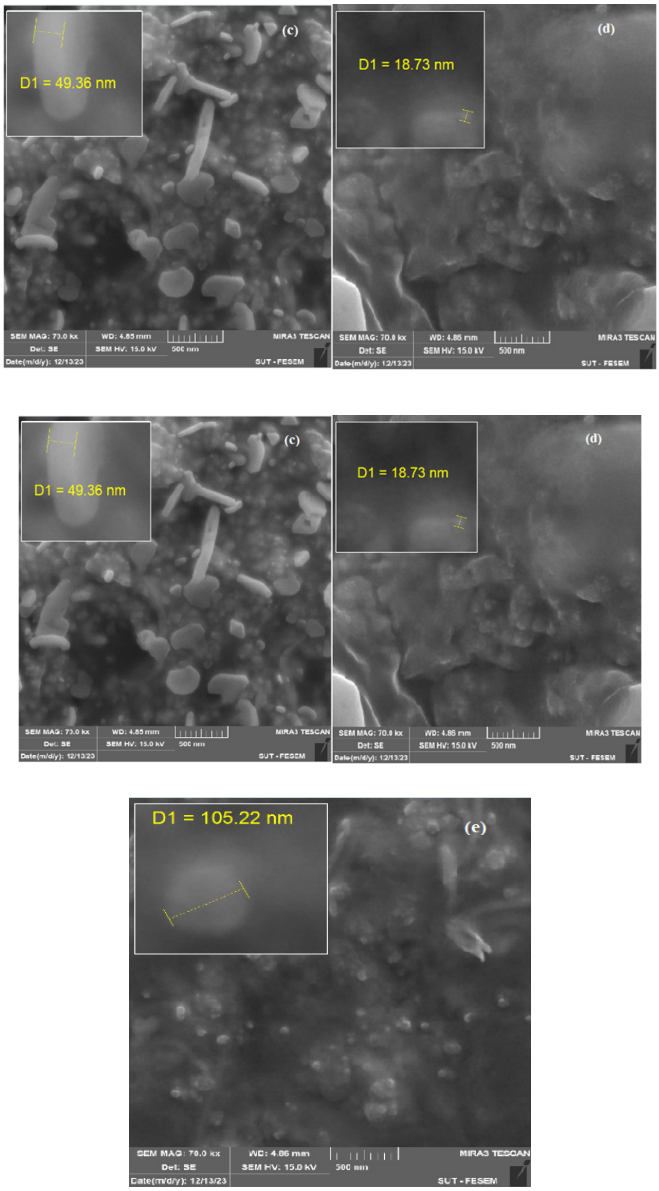

Figure 4: SEM images of GeO_2:SnO_2, (a) GeO_2, (b) GeO_2:2wt%SnO_2, (c) GeO_2:3wt%SnO_2, (d) GeO_2:5wt%SnO_2 and (e) GeO_2:8wt%SnO_2.

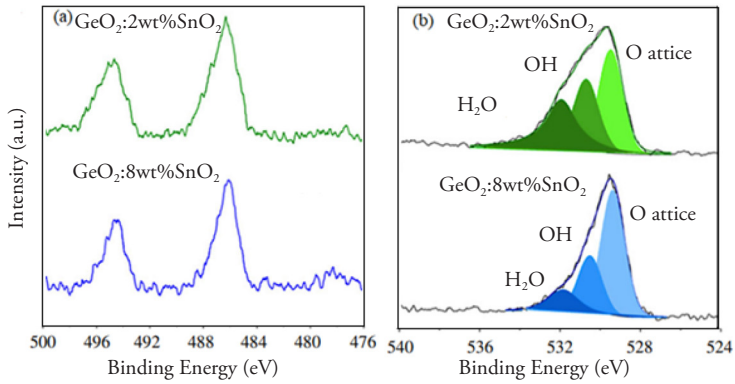

Figure 5: XPS spectra of GeO_2:2 wt.% SnO_2 and GeO_2:8 wt.% SnO_2 thin films in (a) Sn 3d and O 1s, and (b) core-level regions, presented for direct comparison.

Figure 6 illustrates the UV–Vis absorption spectra of GeO_2:SnO_2 thin films deposited on Si substrates at ambient temperature using a laser energy of 350 mJ. All samples exhibited a maximum absorption peak at approximately 290 nm. The absorbance generally increased with increasing SnO_2 doping concentration. In particular, the GeO_2:8 wt% SnO_2 sample showed the highest absorbance value (0.95), while the remaining samples ranged between 0.92 and 0.944 for 0 wt%, 2 wt%, 3 wt% and 5 wt% SnO_2, respectively. The enhanced absorption with higher doping levels may be attributed to modifications in film microstructure and increased defect density, which can enhance light–matter interaction.[27] These observations are consistent with previous reports by Ristoscu et al.[28] Figure 7 presents the optical band gap (E_g) of GeO_2:SnO_2 thin films deposited by PLD at varying SnO_2 concentrations (0 wt%–8 wt%). The band gap was determined by extrapolating the linear region of the Tauc plot ($[\alpha h\nu]^2$ versus $h\nu$). The doping concentration had a pronounced effect on E_g. An initial increase in the band gap was observed at 2 wt% SnO_2 (3.65 eV), followed by a gradual decrease at higher doping levels, reaching 3.45 eV for the 8 wt% SnO_2 sample. The undoped GeO_2 film exhibited an E_g value of 3.55 eV. These findings are in agreement with the results reported by Takane et al.[25] The observed band gap variations can be attributed to competing mechanisms. The initial increase may be associated with improved crystallinity and structural rearrangement, whereas the subsequent decrease at higher doping levels may result from the introduction of defect states or impurity energy levels within the band structure.[29]

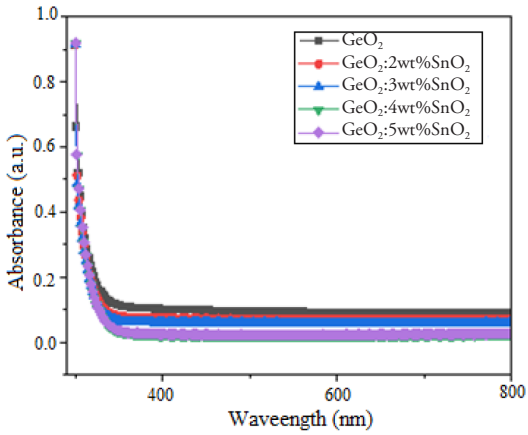

Figure 6: The absorbance of GeO_2:SnO_2 at different ratios at 350 mJ.

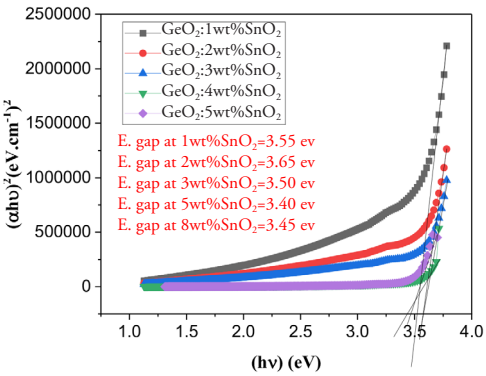

Figure 7: Energy gap of GeO_2:SnO_2 thin films at different ratios at 350 mJ.

The sensing performance of metal oxide thin film sensors are strongly influenced by the film morphology, as the surface structure directly determines the effective area available for gas interaction. Enhanced sensitivity is achieved by maximising the active surface area, where increased surface roughness and optimised grain size provide a higher density of active adsorption sites for NH_3 molecules.[30] In addition, grain boundaries play a crucial role in signal modulation, acting as potential energy barriers whose height changes significantly upon gas exposure.[31] A highly porous structure further promotes efficient gas diffusion and penetration throughout the film, which is essential for achieving rapid response and recovery characteristics.[32] Therefore, precise structural and morphological control is fundamental to optimising gas–solid interactions and improving overall sensing performance (see Figure 8). Figures 9–13 present the real-time resistance response of the GeO_2:SnO_2 gas sensors, demonstrating good reversibility and repeatability. The GeO_2:2 wt% SnO_2 sensor

exhibited a decrease in sensitivity with increasing operating temperature, whereas the GeO_2:8 wt% SnO_2 sensor showed enhanced sensitivity at elevated temperatures. The undoped GeO_2/Si sensor achieved a maximum sensitivity of 20% at 250°C, while the GeO_2:SnO_2/Si composite sensors reached 16% at 300°C. A decline in sensitivity was observed at temperatures above 300°C, which can be attributed to accelerated gas desorption processes.[33] The sensing mechanism is based on resistance variation upon gas exposure, initiated by the adsorption of oxygen species on the surface of GeO_2 and GeO_2:SnO_2 films under ambient air conditions.[34–36]

$$o_2(g) \rightarrow o_2(ads) \tag{2}$$

$$o_2(ads) + e^- \rightarrow o_2^-(ads) o_2^- + e^- \rightarrow 20^-(ads) \tag{3}$$

$$o^- + e^- \rightarrow o_2^- \tag{4}$$

Upon contact to NH_3 gas, hydrogen molecules engage with oxygen ions affixed to the sensor surface, as delineated by the following equation.

$$2NH_3 + 3O^-(ads) \rightarrow N_2 + 3H_2O + 3e^- \tag{5}$$

Upon exposure to NH_3, electrons released from surface reactions reduce the width of the electron depletion layer, leading to a change in electrical resistance and an enhanced sensor response. The adsorption of NH_3, driven by its reducing nature, significantly affects the surface chemistry of the GeO_2:SnO_2 films. All sensors were subjected to identical calcination conditions to ensure comparable physical properties. The sensor response was primarily influenced by the GeO_2–SnO_2 composition and was further enhanced by increasing the SnO_2 doping level and optimising the laser energy during fabrication.[33] Larger grain sizes contributed to improved sensitivity by increasing the effective active surface area and the number of adsorption sites, whereas smaller particles provided fewer active sites, resulting in reduced sensitivity.[37] The calculated sensitivity values are summarised in Table 3. Improved crystallinity was also associated with enhanced sensing performance, as reduced intrinsic resistance facilitates more efficient charge transfer. For example, pure GeO_2 at 250°C and GeO_2:8 wt% SnO_2 at 300°C exhibited relatively high sensitivity (16% for the latter), which can be attributed to their larger grain sizes and increased active surface area, promoting stronger NH_3 interaction.[38] Due to the limited number of recent studies investigating pure GeO_2 as an NH_3 gas sensor at relatively low operating temperatures largely owing to its ultra-wide band gap the comparison table includes the sensing performance of the undoped GeO_2 film from this study as a reference, alongside relevant recent reports on GeO_2-based materials (see Table 4).

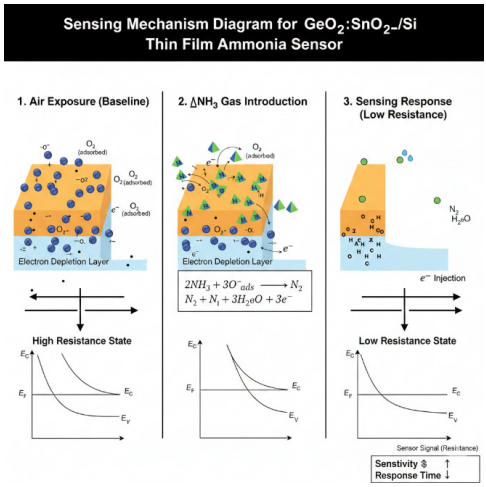

Figure 8: Sensing mechanism diagram for GeO_2: SnO_2/Si thin film ammonia sensor.

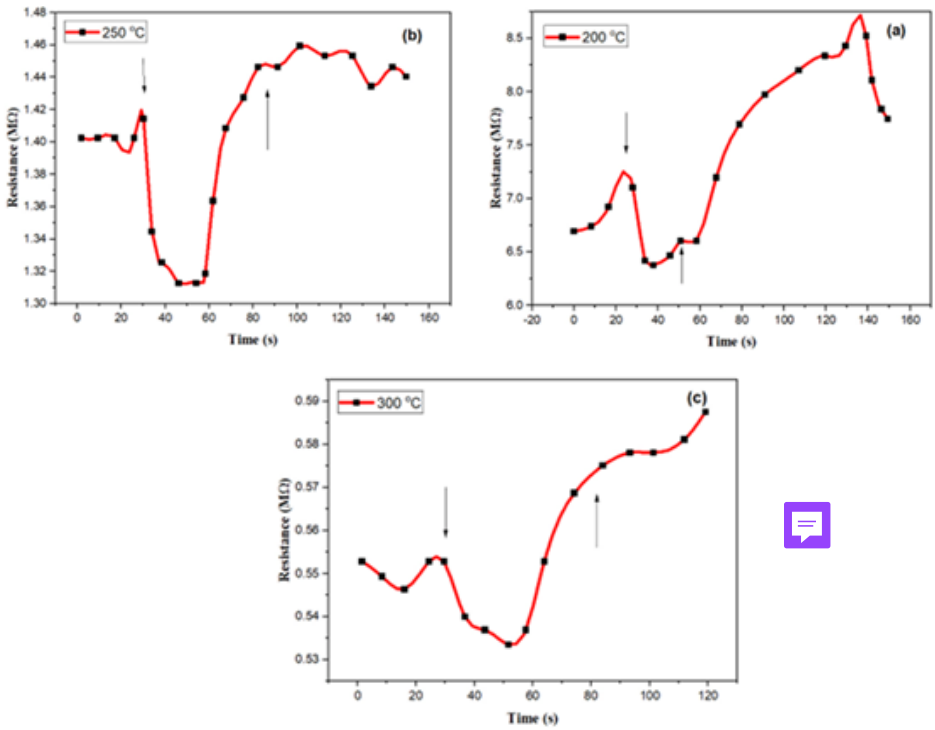

Figure 9: Resistance changes with time of GeO_2 thin film prepared with 350 mJ, for NH_3 gas (a) at 200°C, (b) at 250°C and (c) at 300°C.

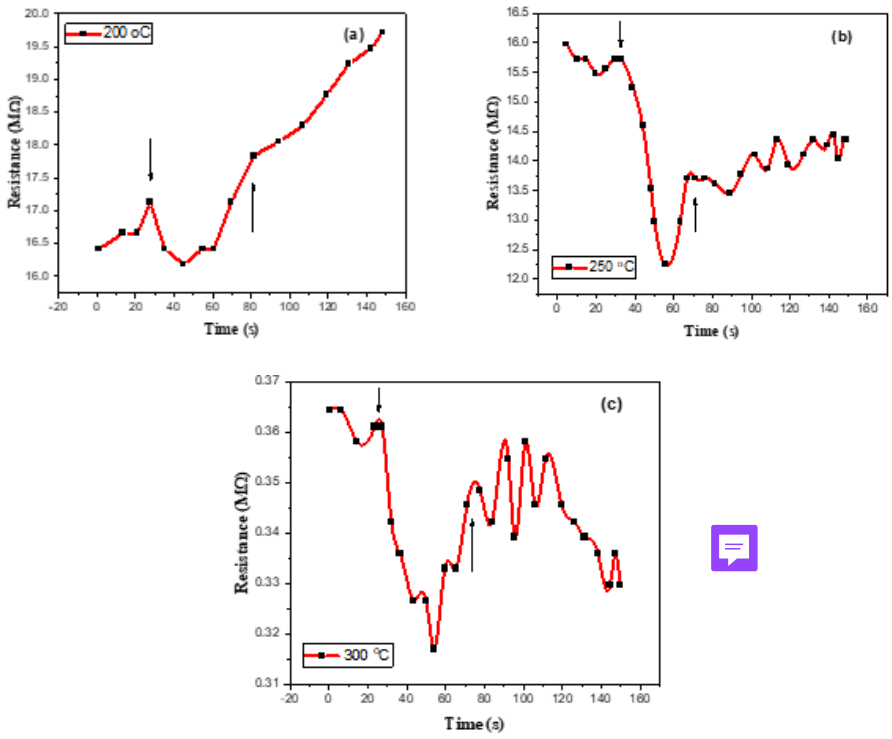

Figure 10: Resistance changes with time of GeO_2:2 wt% SnO_2 thin film prepared with 350 mJ, for NH_3 gas (a) at 200°C, (b) at 250°C and (c) at 300°C.

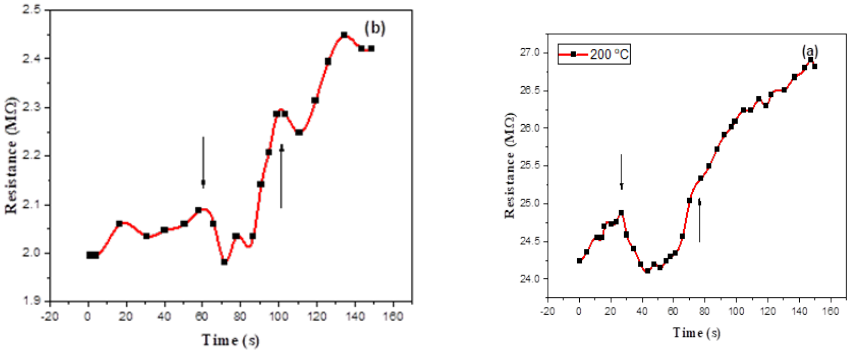

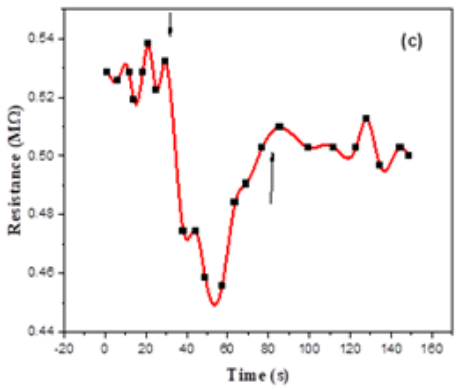

Figure 11: Resistance changes with time of GeO_2:3 wt% SnO_2 thin film prepared with 350 mJ, for NH_3 gas (a) at 200°C, (b) at 250°C and (c) at 300°C.

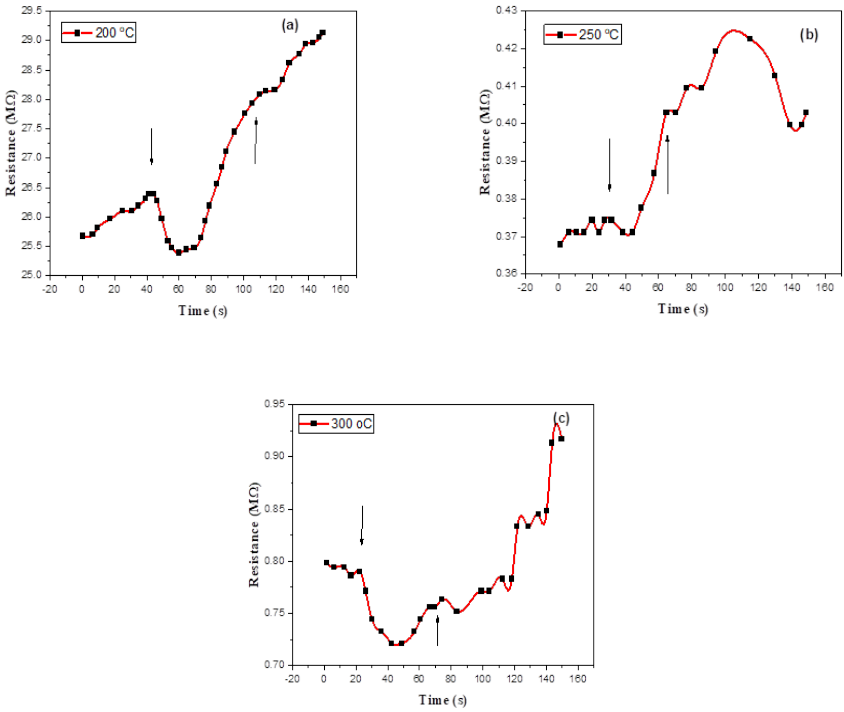

Figure 12: Resistance changes with time of GeO_2:5 wt% SnO_2 thin film prepared with 350 mJ, for NH_3 gas (a) at 200°C, (b) at 250°C and (c) at 300°C.

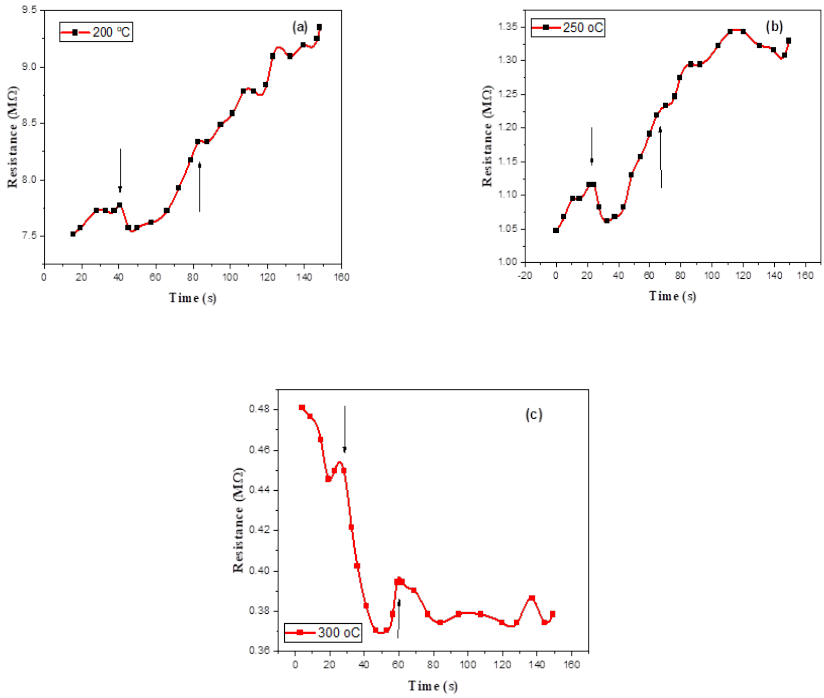

Figure 13: Resistance change with time of GeO_2:8 wt% SnO_2 thin film prepared with 350 mJ, for NH_3 gas (a) at 200°C, (b) at 250°C and (c) at 300°C.

Table 3: The sensing parameters for GeO_2 and GeO_2:SnO_2/n-Si as reducing gas sensors (NH_3)

Name of sample	Operator temperature (°C)	Sensitivity %	Response time (s)	Recovery time (s)
GeO_2 pure	200	4.4	17.6	36.9
	250	5.3	10.3	31.2
	300	15.5	24.7	35.0
GeO_2:2wt%SnO_2/Si	200	4.7	14.1	34.1
	250	11.2	23.3	12.9
	300	11.4	27.6	24.2
GeO_2:3wt%SnO_2/Si	200	3.5	19.0	21.4
	250	12.5	10.8	18.0
	300	11.2	10.5	29.1

(*continue on next page*)

Table 3: (*continued*)

Name of sample	Operator temperature (°C)	Sensitivity %	Response time (s)	Recovery time (s)
GeO_2:5wt%SnO_2/Si	200	4.3	17.2	45.7
	250	3.2	11.7	20.1
	300	8.4	22.5	28.3
GeO_2:8wt%SnO_2/Si	200	3.2	8.4	33.1
	250	2.5	9.3	39.6
	300	16.1	26.1	34.1

Table 4: Comparison of NH_3 gas sensing performance for GeO_2:SnO_2 thin films against GeO_2 based and related literature.

Sensing material	Synthesis method	Test gas / concentration	Operating temperature (°C)	Sensitivity (%)	Ref. (APA In-text)
Pure GeO_2 (This Work)	PLD	NH_3 (100 ppm)	300	~2.5	(This Work)
GeO_2 Nanowires	CVD	CO (200 ppm)	450	~15.0	(Park & Kim, 2022)[40]
GeO_2 (Nanobridge)	Thermal Evaporation	Ethanol (50 ppm)	350	~5.0	(Li et al., 2020)[39]
GeO_2: SnO_2 (8 wt%)	PLD	NH_3 (100 ppm)	300	16.0	(This Work)

4. CONCLUSION

In this study, hexagonal polycrystalline thin films of pure GeO_2 and SnO_2-doped GeO_2 (2 wt%, 3 wt%, 5 wt% and 8 wt%) were successfully fabricated on Si (111) substrates using PLD at a laser energy of 350 mJ with 100 pulses. The incorporation of SnO_2 markedly influenced the structural, morphological, optical and sensing properties of the films. AFM analysis revealed a progressive increase in grain size distribution, surface roughness and RMS values with increasing SnO_2 concentration. SEM showed that the smallest particle size (60.71 nm) was observed for the undoped GeO_2 film, whereas the largest particle size (171.36 nm) was recorded for the 2 wt% SnO_2-doped sample. Optical characterisation indicated that the absorbance reached a maximum value of 0.95 for the 8 wt% SnO_2 film. Concurrently, the optical band gap decreased from 3.55 eV for pure GeO_2 to 3.45 eV with increasing SnO_2 doping concentration. Among all samples, the GeO_2:8 wt% SnO_2 composite exhibited the most promising gas sensing performance, achieving a maximum sensitivity of 16% at an optimal operating temperature of 300°C. Kinetic analysis further demonstrated rapid dynamic

behaviour, with a response time (t_res) of 26.1 s and a recovery time (t_rec) of 34.1 s. The enhanced sensing performance can be attributed to the improved morphological characteristics induced by optimised SnO_2 doping, including increased porosity and larger grain size, which promote efficient gas diffusion and surface reactions.

5. ACKNOWLEDGEMENTS

The authors would like to express their sincere gratitude to University of Mazandaran for their scientific and moral support in completing this research.

6. REFERENCES

1. Kanan, S. et al. (2025). Recent advances on metal oxide based sensors for environmental gas pollutants detection. *Crit. Rev. Anal. Chem.*, 55(5), 911–944. https://doi.org/10.1080/10408347.2024.2325129
2. Zahedi, F. et al. (2014). Structural, optical and electrical properties of ZnO thin films prepared by spray pyrolysis: Effect of precursor concentration. *Bull. Mat. Sci.*, 37(3), 433-439. https://doi.org/10.1007/s12034-014-0696-8
3. Ughade, Y. et al. (2025). Progress in CO_2 gas sensing technologies: Insights into metal oxide nanostructures and resistance-based methods. *Micromach.*, 16(4), 466. https://doi.org/10.3390/mi16040466
4. Kavosh, M. et al. (2024). Improving the FOM of photodetectors fabricated by Sn-doped CuS nanostructures. *Solid State Sci.*, 156, 107653. https://doi.org/10.1016/j.solidstatesciences.2024.107653
5. Thayil, R. & Parne, S. R. (2025). Tuning MoS_2 nanostructures for superior room-temperature toluene sensing. *Talanta Open*, 11, 100402. https://doi.org/10.1016/j.talo.2025.100402
6. Thayil, R. & Parne, S. R. (2025). Nanostructured zinc oxide and selenide-based materials for gas sensing application. *J. Mater. Sci. Mater. Electron.*, 36(5), 1–28.https://doi.org/10.1007/s10854-025-12134-9
7. Khizir, H. A. & Rassam, N. T. (2025). Zn concentration's effects on the structure, optical, and photoconductivity properties of $Zn_xCd_{1-x}S$ thin films synthesized by chemical spray pyrolysis. *J. Korean Phys. Soc.*, 86, 875–883. https://doi.org/10.1007/s40042-024-01242-0
8. Sharmin, A. (2024). Optical and morphological characterization of copper zinc tin sulfide (CZTS) nano-crystal thin film solar cell. PhD diss., University of Dhaka.
9. Yao, L. et al. (2023). Metallophilic interaction-mediated hierarchical assembly and temporal-controlled dynamic chirality inversion of metal–organic supramolecular polymers. *ACS Nano*, 17(3), 2159–2169. https://doi.org/10.1021/acsnano.2c08315

10. Tüzemen, E. Ş. et al. (2023). Experimental and theoretical insights on the structural and optical properties of GeOx thin films deposited via RF magnetron sputtering under varying oxygen percentage. *Physica B Condens Matter*, 650, 414494. https://doi.org/10.1016/j.physb.2023.414494
11. Aounalai, A. (2024). Etude du propriétés optiques des films minces d'oxyde d'étain déposés par spray pyrolyse. PhD. diss., Université de Echahid Cheikh Larbi Tébessi–Tébessa.
12. Zhang, F. et al. (2022). Formation of germanium nanocrystals and amorphous nanoclusters in GeSiOx films using electron beam annealing. *Vacuum*, 197, 110796. https://doi.org/10.1016/j.vacuum.2022.110796
13. Alharbi, S. R., Qasrawi, A. F., & Algarni, S. E. (2021). Effects of Ag_2O nanosheets on the structural, optical, and dielectric properties of GeO_2 stacked layers. *Phys. Status Solidi B-Basic Solid State Phys.*, 258(5), 2000578. https://doi.org/10.1002/pssb.202000578
14. Nalam, P. G. et al. (2022). Controlled phase stabilization enabled tunable optical properties of nanocrystalline GeO_2 films. *ACS Appl. Electron. Mater.*, 4(6), 3115–3124. https://doi.org/10.1021/acsaelm.2c00321
15. Al-Ghamdi, H. et al. (2024). Fabrication, Physical, Structural, Optical Properties, and γ-Ray Attenuation Attributes of Germanate Borosilicate Glasses: Role of GeO_2. *ChemistrySelect*, 9(39), e202402914. https://doi.org/10.1002/slct.202402914
16. Cherkova, S. G. et al. (2021). Optical properties of GeO [SiO] and GeO [SiO2] solid alloy layers grown at low temperature. *Optical Mater.*, 122, 111736. https://doi.org/10.1016/j.optmat.2021.111736
17. Vidhya, D. et al. (2025). Calcium carbide (CaC_2) ripening in fruits: Health risks, non-destructive detection, quality control, and regulatory frameworks. *Compr. Rev. Food Sci. Food Saf.*, 24(2), e70140. https://doi.org/10.1111/1541-4337.70140
18. Saber, S. F. A. (2024). Hydrothermal synthesis of hierarchical nio nanoparticles loaded SnO_2 for acetone gas sensing. Master diss., University of Malaya.
19. Padmashri, P. A. & Aniroodha, P. V. (2014). Nanoparticle films for gas sensing applications: Greener approaches. *J. Environ. Res. Develop.*, 9(1), 945–954.
20. Chen, W. et al. (2025). Kinetics, thermodynamics, and catalysis of the cation incorporation into GeO_2, SnO_2, and (SnxGe1– x) O_2 during suboxide molecular beam epitaxy. *APL Mater.*, 13(1), 011107. https://doi.org/10.1063/5.0203456
21. Patterson, A. L. (1939). The scherrer formula for X-Ray particle size determination. *Phys. Rev.*, 56, 978–982. https://doi.org/10.1103/PhysRev.56.978
22. Wu, J. (2008). Distributed fiber optic gas sensing for harsh environment. General Electric Co., Boston, MA (United States).
23. Sabetzadeh, N. & Gharehaghaji, A. A. (2017). How porous nanofibers have enhanced the engineering of advanced materials: A review. *J. Textiles Polym.*, 5(2), 3–21.
24. Antoja-Lleonart, J. et al. (2021). Growth and crystallization of sio2/geo2 thin films on si (100) substrates. *Nanomater.*, 11(7), 1654. https://doi.org/10.3390/nano11071654
25. Takane, H. et al. (2022). Band-gap engineering of rutile-structured SnO 2-GeO 2-SiO 2 alloy system. *Phys. Rev. Mater.*, 6(8), 084604. https://doi.org/10.1103/PhysRevMaterials.6.084604
26. Szuber, J. et al. (2001). XPS study of the L-CVD deposited SnO_2 thin films exposed to oxygen and hydrogen. *Thin Solid Films*, 391(2), 198–203. https://doi.org/10.1016/S0040-6090(01)00960-0

27. Choi, H. et al. (2023). New heteroleptic germanium precursors for GeO_2 thin films by atomic layer deposition. *ACS Omega*, 8(46), 43759–43770. https://doi.org/10.1021/acsomega.3c05678
28. Bhuiyan, M. M. H. et al.(2008). Improvement in the sensitivity of SnO2 thin film based NOx gas sensor by loading with single-walled carbon nanotube prepared by pulsed laser deposition process. *Sens. Lett.*, 6(4), 635–640. https://doi.org/10.1166/sl.2008.548
29. Takane, H. et al. (2025). Phase-selective synthesis of oxide materials via mist chemical vapor deposition. *Eng. Crystal Habit Appl. Polymorph. Microstext. Learn. Nature.*, 185–198. https://doi.org/10.1007/978-981-96-0266-7_10
30. Liu, M. et al. (2025). Effect of CTAB on the morphology of Sn-MOF and the gas sensing performance of SnO_2 with different crystal phases for H_2 detection. *Chemosens.*, 13(5), 192.
31. Singh, A. et al. (2024). Template-assisted mesoporous SnO_2 based gas sensor for NO_2 detection at low temperature. *J. Porous Mater.*, 31(2), 545–555. https://doi.org/10.1007/s10934-023-01528-0
32. Kaur, N. (2025). Nickel oxide nanostructures for gas sensing: Recent advances, challenges, and future perspectives. *ACS Sens.*, 10(3), 1641–1674. https://doi.org/10.1021/acssensors.4c02946
33. Sheikholeslami, M. (Ed.). (2023). *Nanotechnology applications for solar energy systems*. Wiley & Sons. https://doi.org/10.1002/9781119791232
34. Onizhuk, M. & Galli, G. (2025). *Colloquium*: Decoherence of solid-state spin qubits: A computational perspective. *Rev. Mod. Phys.*, 97(2), 021001. https://doi.org/10.1103/RevModPhys.97.021001
35. Kasap, S. O. (2022). Photoconductivity: fundamental concepts. *Photoconductivity and Photoconductive Materials: Fundamentals, Techniques and Applications*, 1, 1–88. https://doi.org/10.1002/9781119579182.ch1
36. Böer, K. W. & Pohl, U. W. (2023). Optical properties of defects. In *Semiconductor Physics*. Cham: Springer International Publishing, 703–753. https://doi.org/10.1007/978-3-031-23250-9_14
37. Li, Y. et al. (2020). Synthesis and enhanced gas sensing properties of GeO_2 nanobridges. *Sens. Actuators B Chem.*, 325, 128795. https://doi.org/10.1016/j.snb.2020.128795
38. Yan, X. et al. (2025). Water-soluble GeO_2-transferred ultrathin PI/$MnCo_2O_4$/Ta_2O_5 heterostructures for high-sensitivity flexible temperature sensors with extreme stability. *ACS Appl. Mate. Interfaces*, 17(49), 67082–67091. https://doi.org/10.1021/acsami.5c19044